Crystal structures and phase transition in $(Sr_{0.8}Ce_{0.2})(Mn_{1-y}Co_y)O_3$ ($y = 0$ and 0.2): the influence of Jahn–Teller distortion

2009 J. Phys.: Condens. Matter 21 124218

(http://iopscience.iop.org/0953-8984/21/12/124218)

J. Phys.: Condens. Matter **21** (2009) 124218 (8pp) doi:10.1088/0953-8984/21/12/124218

Crystal structures and phase transition in $(Sr_{0.8}Ce_{0.2})(Mn_{1-y}Co_y)O_3$ ($y = 0$ and 0.2): the influence of Jahn–Teller distortion

Zhaoming Zhang[1,5], Christopher J Howard[2], Brendan J Kennedy[3], Motohide Matsuda[4] and Michihiro Miyake[4]

[1] Institute of Materials Engineering, Australian Nuclear Science and Technology Organisation, Lucas Heights, NSW 2234, Australia
[2] School of Engineering, The University of Newcastle, Callaghan, NSW 2308, Australia
[3] School of Chemistry, The University of Sydney, Sydney, NSW 2006, Australia
[4] Graduate School of Environmental Science, Okayama University, 3-1-1 Tsushima-Naka, Okayama 700-8530, Japan

E-mail: zhaoming.zhang@ansto.gov.au

Received 25 September 2008, in final form 29 October 2008
Published 25 February 2009
Online at stacks.iop.org/JPhysCM/21/124218

Abstract

We have studied the crystal structures of $(Sr_{0.8}Ce_{0.2})(Mn_{1-y}Co_y)O_3$ ($y = 0$ and 0.2) using neutron diffraction. Both $(Sr_{0.8}Ce_{0.2})MnO_3$ and $(Sr_{0.8}Ce_{0.2})(Mn_{0.8}Co_{0.2})O_3$ have a tetragonal structure in space group $I4/mcm$ at room temperature, and the octahedral tilt angle around the c-axis is nearly the same. The only significant difference is the shape of the $Mn(Co)O_6$ octahedron: it is elongated in $(Sr_{0.8}Ce_{0.2})MnO_3$ due to the cooperative Jahn–Teller (JT) effect, but essentially regular in $(Sr_{0.8}Ce_{0.2})(Mn_{0.8}Co_{0.2})O_3$ due to the absence of JT-active Mn^{3+} ions. With increasing temperature, both compounds undergo a continuous phase transition at around 400 °C to a cubic structure in $Pm\bar{3}m$, with no indication of a distinct transition in $(Sr_{0.8}Ce_{0.2})MnO_3$ from the removal of the static JT distortion. In addition, the temperature dependence of the octahedral tilt angle is very similar in the two samples, implying that the JT distortion has minimal effect on the octahedral tilting and the phase transition to cubic. X-ray absorption near-edge structure (XANES) analysis indicates that the Ce oxidation state is predominantly 4+ in both samples. The electrical conductivity is higher in $(Sr_{0.8}Ce_{0.2})MnO_3$ than in $(Sr_{0.8}Ce_{0.2})(Mn_{0.8}Co_{0.2})O_3$ in the temperature range studied (100–900 °C).

(Some figures in this article are in colour only in the electronic version)

1. Introduction

Perovskite-type manganites are a class of materials that show fascinating properties, largely due to the fine balance among the spin, charge and orbit ordering in these materials (Mathur and Littlewood 2003). Although early studies of manganites date back to the 1950s, recent interest in these materials has been sparked by the discovery of colossal magnetoresistance (CMR) in hole-doped manganites $R_{1-x}A_xMnO_3$ with mixed Mn^{3+}/Mn^{4+} ions (R = trivalent lanthanide and A = divalent ions such as Ca and Sr) (Jin *et al* 1994). In addition, strontium-doped lanthanum manganite perovskite (LSM) is also the most commonly used cathode material for solid oxide fuel cells (SOFC) (Skinner 2001).

Although hole-doped manganites (Mn^{3+}-rich) have been studied extensively, the electron-doped materials $A_{1-x}R_xMnO_3$ (Mn^{4+}-rich) have received relatively little attention. One of the interesting systems is the electron-doped series $Sr_{1-x}Ce_xMnO_3$, which was suggested as a potential cathode material. Compared to LSM, Ce-doped $SrMnO_3$ is cheaper, and exhibits higher conductivity (Hashimoto and

[5] Author to whom any correspondence should be addressed.

Iwahara 2000a, 2000b). In addition, these materials are compatible with CeO_2-based electrolytes (Hashimoto and Iwahara 2000a, 2000b). The $Sr_{1-x}Ce_xMnO_3$ series also displays interesting structural transitions with increasing Ce-doping. Pure $SrMnO_3$ has a four-layer hexagonal structure at temperatures below 1035 °C (Negas and Roth 1970). The substitution of a small amount of Ce for Sr can stabilize the ideal cubic perovskite structure, e.g. in $Sr_{0.95}Ce_{0.05}MnO_3$ (Wu *et al* 2007) and $Sr_{0.925}Ce_{0.075}MnO_3$ (Kennedy *et al* 2008a). To maintain charge neutrality, some Mn^{4+} ions are reduced to Mn^{3+}, introducing Jahn–Teller (JT) active $Mn^{3+}(d^4)$ ions. With the increase of Ce content, a transition to a tetragonal structure is observed at $x \sim 0.1$ (Sundaresan *et al* 2000, Kennedy *et al* 2008a). This phase transition is brought about by cooperative Jahn–Teller distortions (CJTD). However, as the Ce content (hence JT-active Mn^{3+}) increases further, the cell metric distortion (i.e. c/a ratio) decreases while the MnO_6 octahedral tilt angle increases until an orthorhombic structure forms at $x \sim 0.35$ (Kennedy *et al* 2008a). This apparent disjoint between the cell metric and internal distortion is quite intriguing.

In order to investigate the effect of JT distortion on the structure, we have carried out neutron diffraction studies of two manganite samples: $(Sr_{0.8}Ce_{0.2})MnO_3$ and $(Sr_{0.8}Ce_{0.2})(Mn_{0.8}Co_{0.2})O_3$. These two samples have a similar tolerance factor (t), but only the former is expected to contain JT-active Mn^{3+} ions. A comparative study of this pair of samples provides an excellent opportunity to separate the effects of the JT distortion and the octahedral tilting distortion. Furthermore, because strontium-doped lanthanum cobaltate perovskites (LSC) have good oxide ion conductivity whereas the manganites have favourable electronic conductivity (Skinner 2001), it is hoped that Co-doping on the Mn-site in Ce-doped strontium manganite might lead to improved conductivity. In an attempt to explore the possibility of these samples as potential cathode materials for SOFC applications, the electrical conductivity was measured from $(Sr_{0.8}Ce_{0.2})(Mn_{1-y}Co_y)O_3$ ($y = 0$ and 0.2) in the temperature range of 100–900 °C.

2. Experimental details

The samples were prepared by standard solid-state reaction methods. Powders of $SrCO_3$ (Kantou kagaku, 99.9%), CeO_2 (Kantou kagaku, 99.99%), Mn_3O_4 (Koujundo kagaku, 99.9%) and Co_3O_4 (Kantou kagaku, 99.95%) were weighed at stoichiometric proportions and mixed for 24 h using a ball mill. The mixture was calcined at 800 °C for 10 h in air. The calcined powder was then sufficiently crushed in the ball mill for 24 h, sintered at 1400 °C for 10 h in air and furnace cooled to room temperature. The crystallinity and phase purity of the samples were checked using laboratory powder x-ray diffraction with Cu Kα radiation. The samples were also analysed using a JEOL 6400 scanning electron microscope fitted with an energy dispersive spectrometer. This verified the sample compositions and showed them to be homogeneous solid solutions. The sintered powders were pelletized and annealed at 1300 °C for 8 h before neutron diffraction measurements.

Time-of-flight neutron diffraction patterns were recorded using the instrument Polaris at the ISIS neutron facility, Rutherford Appleton Laboratory, UK (Smith and Hull 1997). The samples were loaded into thin-walled 11 mm diameter vanadium sample cans and mounted in an ISIS designed 1000 °C furnace which employs a cylindrical vanadium element and operates under high vacuum. Temperatures were monitored and controlled using two type-K thermocouples, one located close to the furnace element, the other mounted on the sample stick and placed in contact with the sample can. Diffraction data were obtained from the back-scattering bank, recording d-spacings from 0.3 to 3.2 Å at a resolution $\Delta d/d \sim 5 \times 10^{-3}$. The time-of-flight data were first converted to d-spacing, and summed, to produce a single pattern. Then, after subtracting an instrumental background, the patterns were normalized by dividing by a spectrum derived from the measurement of incoherent scattering from a vanadium rod (to account for the variation with neutron wavelength of both the incident flux and the detector efficiency). Patterns were recorded to a total incident proton beam of 135 μA h at room temperature and 100 °C, corresponding to about 45 min beamtime. In order to obtain accurate oxygen occupancy at elevated temperatures, diffraction patterns were collected for a total incident proton beam of 180 μA h at 500, 600, 700 and 800 °C. All other data were recorded to a minimum total incident proton beam of 45 μA h.

The neutron diffraction patterns were fitted using the Rietveld method (Rietveld 1969) as implemented in the GSAS computer program (Larson and von Dreele 1994, Toby 2001). The peak shapes were modelled as convolutions of back-to-back exponentials with a pseudo-Voigt in which two peak width parameters were varied, and the background as Chebyshev polynomials (Larson and von Dreele 1994). Displacement parameters were refined along with internal coordinates, and oxygen displacement parameters were taken to be anisotropic. The isotropic displacement parameters for the two A-site cations (Sr and Ce) were constrained to be equal, so were those for the two B-site cations (Mn and Co). The oxygen occupancy in the high temperature cubic phase was also refined, to monitor the possible presence of anion vacancies (but none were found). Certain peaks seen to be broadened (R-point peaks—see section 3.1 below) were distinguished using the 'stacking fault' model within the GSAS computer program (Larson and von Dreele 1994), and then fitted with larger peak widths than the rest of the peaks.

X-ray absorption near-edge structure (XANES) analysis was carried out at beamline 16A1 at the National Synchrotron Radiation Research Center (NSRRC) in Hsinchu, Taiwan (Dann *et al* 1998). The Ce $L_{3,2}$- and Mn K-edge spectra were measured in fluorescence mode using a Lytle detector from powder samples dispersed on Kapton tape. Energy steps as small as 0.2 eV were employed near the absorption edges with a counting time of 2 s per step. The energy scale was calibrated using the K-edge of a pure Mn foil at 6539 eV. The spectra were normalized to the incident photon current, but no background removal was performed. The electrical conductivity was measured by the four-point probe DC method upon cooling the samples from 900 to 100 °C in air.

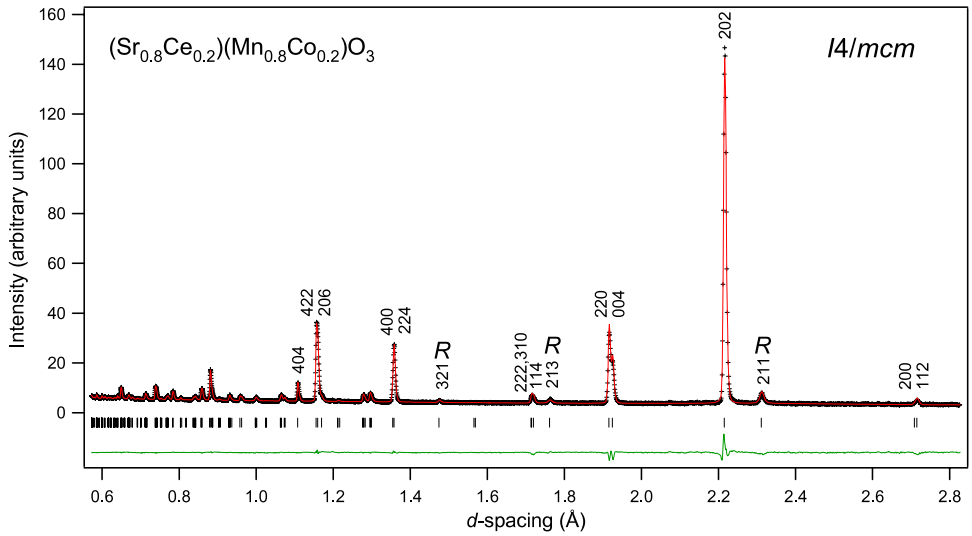

Figure 1. Neutron diffraction pattern recorded at room temperature from $(Sr_{0.8}Ce_{0.2})(Mn_{0.8}Co_{0.2})O_3$. The crosses represent the observed data, and the continuous line is the fit obtained by the Rietveld method using the tetragonal structure in $I4/mcm$. The vertical marks show the peak positions expected in this structure, and the line beneath the pattern records the difference between the observed and calculated patterns. The peaks in the figure are identified by indices based on the $\sqrt{2} \times \sqrt{2} \times 2$ cell.

Table 1. Refined lattice parameters, Wyckoff sites, fractional atomic coordinates, occupancies and displacement parameters (10^{-2} Å^2) for $(Sr_{0.8}Ce_{0.2})(Mn_{0.8}Co_{0.2})O_3$ at room temperature and 500 °C. The number in parentheses beside each entry indicates the estimated standard deviation referred to the last digit shown.

Atom	Site	x	y	z	Occupancy	Uiso/U^{11}	U^{22}	U^{33}	U^{12}	U^{13}	U^{23}
Room temperature: $I4/mcm$, $a = b = 5.4171(1)$, $c = 7.6972(1)$ Å, $R_{wp} = 1.46\%$, $R_p = 2.68\%$											
Sr/Ce	4b	0	0.5	0.25	0.8/0.2	0.655(12)					
Mn/Co	4c	0	0	0	0.8/0.2	0.435(15)					
O1	4a	0	0	0.25	1	2.357(42)	=U^{11}	0.87(6)	0	0	0
O2	8h	0.2261(1)	$=x+0.5$	0	1	1.039(16)	=U^{11}	2.76(5)	0.581(24)	0	0
500 °C: $Pm\bar{3}m$, $a = b = c = 3.860\,92(1)$ Å, $R_{wp} = 1.17\%$, $R_p = 2.07\%$											
Sr/Ce	1b	0.5	0.5	0.5	0.8/0.2	1.522(16)					
Mn/Co	1a	0	0	0	0.8/0.2	0.782(18)					
O	3d	0	0.5	0	1	4.126(19)	1.139(24)	=U^{11}	0	0	0

Table 2. Axial (Mn–O1) and equatorial (Mn–O2) bond lengths in $(Sr_{0.8}Ce_{0.2})MnO_3$ and $(Sr_{0.8}Ce_{0.2})(Mn_{0.8}Co_{0.2})O_3$, as obtained from the analysis of room temperature neutron data. Δd is a measure of the octahedral distortion.

	Mn–O1 (Å)	Mn–O2 (Å)	$\Delta d = (1/6)\sum[(d_n - d)/d]^2$
$(Sr_{0.8}Ce_{0.2})MnO_3$	1.933 70(2)	1.925 07(9)	4.4×10^{-6}
$(Sr_{0.8}Ce_{0.2})(Mn_{0.8}Co_{0.2})O_3$	1.924 30(3)	1.923 99(9)	5.8×10^{-9}

3. Results and discussions

3.1. Crystal structure at room temperature

The neutron diffraction patterns obtained at room temperature from both $(Sr_{0.8}Ce_{0.2})MnO_3$ and $(Sr_{0.8}Ce_{0.2})(Mn_{0.8}Co_{0.2})O_3$ are similar; the pattern from the latter is shown in figure 1. A close inspection of the patterns reveals that the structure is tetragonal in space group $I4/mcm$. This is the same structure as that reported for $(Sr_{0.8}Ce_{0.2})MnO_3$ (Sundaresan *et al* 2000, Lu *et al* 2005, Kennedy *et al* 2008a). The tilt system is described in Glazer's notation (Glazer 1972) as $a^0a^0c^-$, indicating out-of-phase tilt around the c-axis. Refinements were carried out and the results for $(Sr_{0.8}Ce_{0.2})(Mn_{0.8}Co_{0.2})O_3$ are listed in table 1. It is worthwhile mentioning that the R-point superlattice peaks are broader than the main perovskite peaks. Recalling that the R-point superlattice reflections arise from out-of-phase tilting of the Mn(Co)O_6 octahedra, we attribute this broadening to the occasional reversal of the sense of this tilt (i.e. the tilting of octahedra in the next plane along the tilting axis is occasionally in the same sense, rather than in the opposite sense as required for out-of-phase tilting). This could occur within an otherwise unaltered framework and so not impact on the other peaks. In other words, we believe this to be a kind of (domain) size broadening, reflecting that the coherence of the out-of-phase octahedral

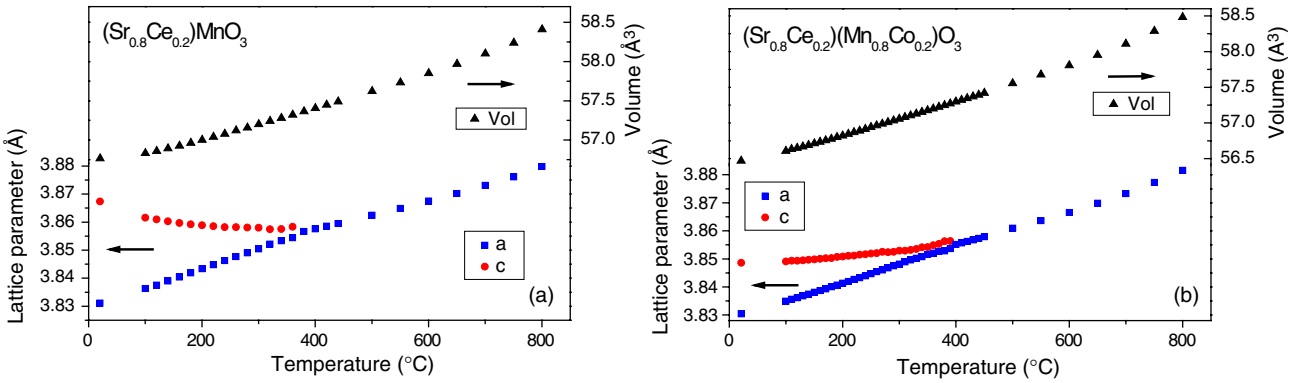

Figure 2. Temperature dependence of the equivalent primitive cell volume and appropriately scaled lattice parameters for (a) $(Sr_{0.8}Ce_{0.2})MnO_3$, and (b) $(Sr_{0.8}Ce_{0.2})(Mn_{0.8}Co_{0.2})O_3$. Note the lattice parameter at 800 °C in (b) was obtained from refining the first 15 min diffraction pattern.

tilting is maintained over only a rather limited range. The magnitude of octahedral tilting can be estimated from the oxygen coordinate, $\phi = \tan^{-1}[1 - 4x(O2)]$. The tilt angle at room temperature is very similar for both materials: 5.7° for $(Sr_{0.8}Ce_{0.2})MnO_3$ and 5.5° for $(Sr_{0.8}Ce_{0.2})(Mn_{0.8}Co_{0.2})O_3$. The shape of the octahedra, however, differs. As shown in table 2, the MnO_6 octahedra in $(Sr_{0.8}Ce_{0.2})MnO_3$ are elongated with two long and four short Mn–O bonds, which is attributed to cooperative Jahn–Teller (JT) effects (due to the presence of JT-active Mn^{3+} ions). On the other hand, the $Mn(Co)O_6$ octahedra in $(Sr_{0.8}Ce_{0.2})(Mn_{0.8}Co_{0.2})O_3$ is essentially regular in shape, indicating the absence of static Jahn–Teller distortion. This is consistent with the view that no JT-active Mn^{3+} ions are expected in $(Sr_{0.8}Ce_{0.2})(Mn_{0.8}Co_{0.2})O_3$ (see discussions in section 3.2, below). The distortion of octahedra can also be quantified using the quantity $\Delta d = (1/6)\sum[(d_n - d)/d]^2$ where d is the mean Mn(Co)–O distance and d_n the individual Mn(Co)–O distance (Rodríguez-Carvajal *et al* 1998); Δd has a value three orders of magnitude lower for the Co-doped sample.

3.2. Variable temperature studies

Neutron diffraction patterns were recorded from both $(Sr_{0.8}Ce_{0.2})MnO_3$ and $(Sr_{0.8}Ce_{0.2})(Mn_{0.8}Co_{0.2})O_3$ from 100 to 800 °C. As expected, both the magnitude of the tetragonal splitting (or broadening where not resolved) and the intensity of R-point reflections decrease with increasing temperature. Upon close inspection of the R-point reflections, it appears that the structure is cubic at 380 °C for $(Sr_{0.8}Ce_{0.2})MnO_3$ and 400 °C for $(Sr_{0.8}Ce_{0.2})(Mn_{0.8}Co_{0.2})O_3$, which are consistent with the transition temperatures obtained from strain analysis (see figure 3 below). Structure refinements were carried out for all temperature runs using the same protocol as described earlier. Diffraction patterns obtained at temperatures above the transition were refined using the cubic structure in $Pm\bar{3}m$ ($a^0a^0a^0$). Details of the cubic structure at 500 °C for $(Sr_{0.8}Ce_{0.2})(Mn_{0.8}Co_{0.2})O_3$ are also included in table 1. In order to monitor any possible vacuum-induced reduction at 600, 700 and 800 °C, the 1 h diffraction pattern collected at each of these three temperatures consisted of four consecutive

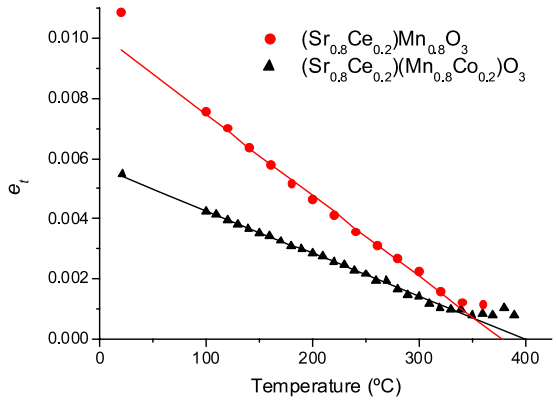

Figure 3. Temperature dependence of tetragonal strain for $(Sr_{0.8}Ce_{0.2})MnO_3$ and $(Sr_{0.8}Ce_{0.2})(Mn_{0.8}Co_{0.2})O_3$. Note that the linear extrapolation does not include data points at RT and 340–360 °C for $(Sr_{0.8}Ce_{0.2})MnO_3$, or at 360–390 °C for $(Sr_{0.8}Ce_{0.2})(Mn_{0.8}Co_{0.2})O_3$.

15 min patterns, and the refinements (including the oxygen-site occupancy) were carried out for each of the 15 min patterns as well as the summed 1 h pattern. All results are indistinguishable except those for $(Sr_{0.8}Ce_{0.2})(Mn_{0.8}Co_{0.2})O_3$ at 800 °C, where a very small amount of oxygen vacancies (~0.5%) was detected. As a result of this vacuum-induced reduction, the lattice parameter increased from 3.8816 to 3.8827 Å over a period of 1 h. No oxygen vacancies were detected up to 800 °C for $(Sr_{0.8}Ce_{0.2})MnO_3$. It should be mentioned that the very wide Q range accessible on Polaris is invaluable in the refinement of O-site occupancies.

Figures 2(a) and (b) show the temperature dependence of the lattice parameters and the cell volume for $(Sr_{0.8}Ce_{0.2})MnO_3$ and $(Sr_{0.8}Ce_{0.2})(Mn_{0.8}Co_{0.2})O_3$ respectively, suggesting that the thermally induced $I4/mcm \leftrightarrow Pm\bar{3}m$ transition is a continuous one. The most obvious difference between the two samples is the temperature dependence of lattice parameter c in the tetragonal phase: one contracts with increasing temperature [$(Sr_{0.8}Ce_{0.2})MnO_3$], whereas the other expands [$(Sr_{0.8}Ce_{0.2})(Mn_{0.8}Co_{0.2})O_3$]. The contraction of c in $(Sr_{0.8}Ce_{0.2})MnO_3$ is typical for samples with static JT

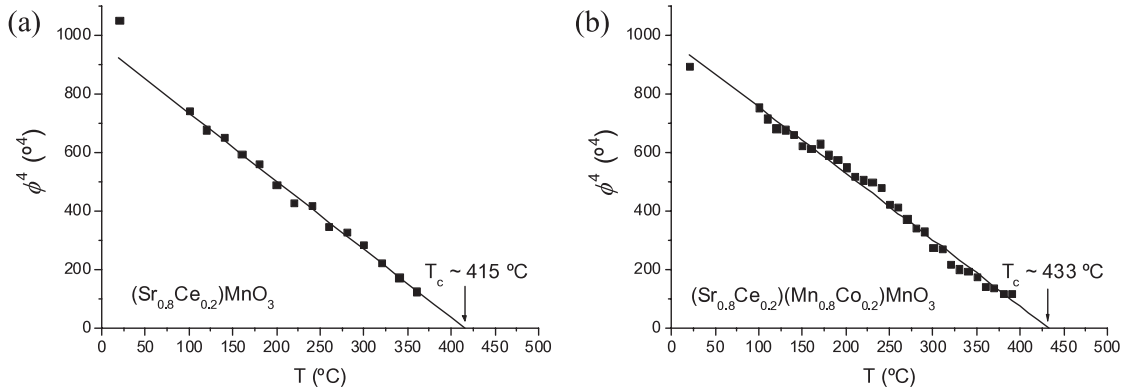

Figure 4. Temperature dependence of the fourth power of the octahedral tilt angle for (a) $(Sr_{0.8}Ce_{0.2})MnO_3$ and (b) $(Sr_{0.8}Ce_{0.2})(Mn_{0.8}Co_{0.2})O_3$. The solid lines are linear fits to the data, giving $T_c \approx 415\,^{\circ}C$ for $(Sr_{0.8}Ce_{0.2})MnO_3$ and $433\,^{\circ}C$ for $(Sr_{0.8}Ce_{0.2})(Mn_{0.8}Co_{0.2})O_3$. Note that the linear fit in (a) does not include the RT data point, as it was obtained during a separate trip.

distortions (Kennedy and Zhou 2008). The absence of such distortions in $(Sr_{0.8}Ce_{0.2})(Mn_{0.8}Co_{0.2})O_3$ suggests that Co-doping destroys the cooperative JT effect in $(Sr_{0.8}Ce_{0.2})MnO_3$. This could be a result of two scenarios: either there is no JT-active Mn^{3+} in $(Sr_{0.8}Ce_{0.2})(Mn_{0.8}Co_{0.2})O_3$, or the JT distortion in this sample is a dynamic one. In order to distinguish between these two possibilities, we have examined the oxygen displacement parameters of the two samples with and without Co-doping. The results revealed that the oxygen displacement parameters of $(Sr_{0.8}Ce_{0.2})(Mn_{0.8}Co_{0.2})O_3$ are comparable to those of $(Sr_{0.8}Ce_{0.2})MnO_3$ at all temperatures (in both the tetragonal and cubic phases), and their values increase very nearly linearly with temperature (as do the displacement parameters of cations). This suggests that there are no JT-active Mn^{3+} ions in the Co-doped sample, as dynamic JT distortions are expected to lead to a significant increase in the displacement parameters of oxygen atoms (Rodríguez-Carvajal *et al* 1998, Chatterji *et al* 2002). This conclusion is also consistent with the Mn K-edge XANES spectra of the two samples (see figure 6 below).

From the lattice parameters we can derive the spontaneous strains, with the symmetry-breaking strain as $e_t = 2(c - a)/\sqrt{3}a_0$, where a and c are lattice parameters of the reduced cell for the tetragonal structure, and a_0 is the reference parameter of the cubic structure extrapolated into the tetragonal stability field (approximated using $a_0 \approx (2a + c)/3$) (Carpenter *et al* 2006, Howard *et al* 2007). Figure 3 shows the tetragonal strain (e_t) as a function of temperature for both $(Sr_{0.8}Ce_{0.2})MnO_3$ and $(Sr_{0.8}Ce_{0.2})(Mn_{0.8}Co_{0.2})O_3$. Due to the fact that the determination of lattice parameters is always problematic at temperatures approaching a continuous phase transition, the strain data are not as reliable at temperatures just below the transition. However, when these data points are excluded, the strain is seen to vary linearly with temperature with an extrapolation to zero at 378 and 401 °C for $(Sr_{0.8}Ce_{0.2})MnO_3$ and $(Sr_{0.8}Ce_{0.2})(Mn_{0.8}Co_{0.2})O_3$, respectively. (Note: the linear fit for $(Sr_{0.8}Ce_{0.2})MnO_3$ also excluded the data point at room temperature (RT) because the diffraction pattern was obtained during a previous trip to ISIS.) These transition temperatures are consistent with those obtained from monitoring the disappearance of *R*-point reflections; the transition temperature obtained for $(Sr_{0.8}Ce_{0.2})MnO_3$ in this study is also in good agreement with that obtained from a previous synchrotron x-ray study (~385 °C) (Kennedy *et al* 2008a).

As shown in figure 3, the tetragonal strain in $(Sr_{0.8}Ce_{0.2})MnO_3$ is higher than that in $(Sr_{0.8}Ce_{0.2})(Mn_{0.8}Co_{0.2})O_3$ until a temperature just below the transition to cubic. This is attributed to the additional strain resulting from the cooperative JT distortion in $(Sr_{0.8}Ce_{0.2})MnO_3$. Another interesting observation from the tetragonal strain in $(Sr_{0.8}Ce_{0.2})MnO_3$ is that the slope of the temperature dependence does not change, indicating that the transition due to the removal of JT distortion coincides with that from the loss of cooperative octahedral tilting. This is in contrast to other manganites such as $SrRu_{0.5}Mn_{0.5}O_3$ (Kennedy and Zhou 2008) and $Sr_{0.9-x}Ca_xCe_{0.1}MnO_3$ (Kennedy *et al* 2008b), where there are two distinct transitions—first due to the removal of orbital ordering and the second the loss of octahedral tilting.

The nature of the continuous phase transition can be established by examining the temperature dependence of an appropriate order parameter (Q), e.g. $Q = A(T_c - T)^n$ with $n = 1/2$ or $1/4$ for a second order or tricritical transition, respectively (Salje 1990). For tilting transitions in perovskites, the order parameter Q can be represented by the octahedral tilt angle. As shown in figure 4, ϕ^4 varies linearly with temperature with an extrapolation to zero at $T_c \approx 415$ and 433 °C for $(Sr_{0.8}Ce_{0.2})MnO_3$ and $(Sr_{0.8}Ce_{0.2})(Mn_{0.8}Co_{0.2})O_3$, respectively. These results clearly indicate that the tetragonal to cubic transition is tricritical in nature (Salje 1990), i.e. $\phi = A(T_c - T)^{1/4}$. It is evident that the transition temperature extrapolated from the tilt angles is higher than that obtained from the strain analysis. This was reported previously for $BaBiO_3$ and Ba_2BiSbO_6 (Kennedy *et al* 2006) and $Nd_{1/3}NbO_3$ (Zhang *et al* 2007), and was attributed to an average angle of dynamical tilting at the transition. Therefore it would be more reliable to estimate the transition temperature from the strain analysis.

Since both e_t (figure 3) and ϕ^4 (figure 4) scale linearly with temperature, e_t also varies linearly with ϕ^4. However, the general relationship between the two is either $e_t \propto \phi$ (when the

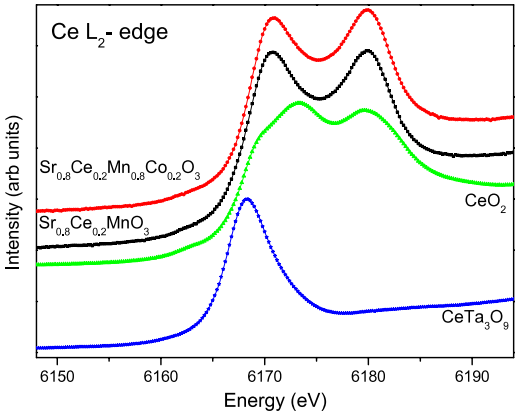

Figure 5. Ce L_2-edge XANES spectra of $(Sr_{0.8}Ce_{0.2})MnO_3$, $(Sr_{0.8}Ce_{0.2})(Mn_{0.8}Co_{0.2})O_3$, $CeTa_3O_9$ (Ce^{3+} standard) and CeO_2 (Ce^{4+} standard).

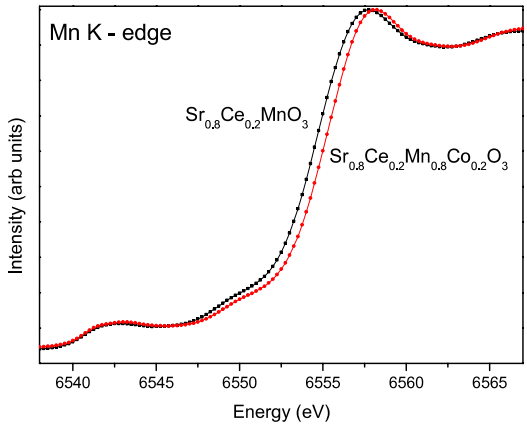

Figure 6. Mn K-edge XANES spectra of $(Sr_{0.8}Ce_{0.2})MnO_3$ and $(Sr_{0.8}Ce_{0.2})(Mn_{0.8}Co_{0.2})O_3$.

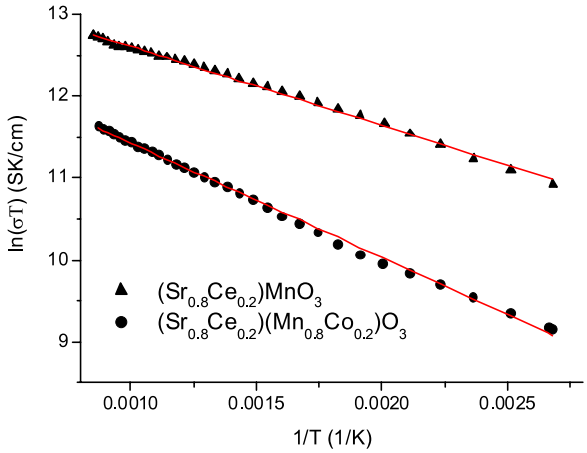

Figure 7. The relationship between $\ln(\sigma T)$ and $1/T$ for $(Sr_{0.8}Ce_{0.2})MnO_3$ and $(Sr_{0.8}Ce_{0.2})(Mn_{0.8}Co_{0.2})O_3$. The linear fit is based on the 'small polaron hopping' model $\sigma = (C/T)\exp(-E_h/kT)$.

symmetry-breaking strain and order parameter have the same symmetry), or $e_t \propto \phi^2$ (for all other strains), because higher-order coupling terms in the Landau free-energy expansion can usually be neglected relative to the lowest-order coupling term allowed by symmetry (Carpenter *et al* 1998). This assumption is obviously not valid in the current case, where the dominant coupling term seems to arise from higher-order terms. Other materials with higher-order coupling, including $BaCeO_3$ perovskite, were also reported by Carpenter *et al* (1998). Given that the higher-order coupling terms cannot always be neglected, the simple relationship between the strain (e) and the order parameter (Q) ($e \propto Q$ or $e \propto Q^2$) is not always true. In such circumstances the nature of a continuous phase transition is better determined from the temperature dependence of the order parameter, not that of the strain.

We also recorded a neutron diffraction pattern from $(Sr_{0.8}Ce_{0.2})MnO_3$ at 4 K to check for possible low temperature phases. But this pattern was very well fitted assuming the same $I4/mcm$ structure with lattice parameters $a = b = 5.4052(1)$ and $c = 7.7636(1)$ Å, and the octahedral tilt angle increased to 6.1°.

3.3. XANES results

Although it is agreed in the literature that the cerium ions in $Ca_{1-x}Ce_xMnO_3$ are in a tetravalent state (i.e. the substitution of each Ce^{4+} ion for Ca^{2+} is charge-compensated by the reduction of two Mn^{4+} to Mn^{3+}) (Zeng *et al* 2001, Maignan *et al* 1998), there is no consensus on the oxidation state of Ce in $Sr_{1-x}Ce_xMnO_3$. Whereas Sundaresan *et al* (2000) reported the presence of Ce^{3+} (as indicated by their magnetic measurements), Mandal *et al* (2004) suggested Ce^{4+} in their $Sr_{1-x}Ce_xMnO_3$ samples. It should be mentioned that the structural sequence reported by these two groups was also different, which was attributed by Mandal *et al* (2004) to the differences in sample preparation details.

Figure 5 shows the Ce L_2-edge XANES spectra of $(Sr_{0.8}Ce_{0.2})MnO_3$ and $(Sr_{0.8}Ce_{0.2})(Mn_{0.8}Co_{0.2})O_3$ along with those of the Ce^{3+} ($CeTa_3O_9$) and Ce^{4+} (CeO_2) standards (the Ce L_3-edge XANES spectra were also obtained, and show similar features to those of the Ce L_2-edge). The Ce $L_{3,2}$-edge spectra result from dipole transitions of the Ce 2p electrons into the empty d- and s-states mixed in the conduction band, i.e. probing the unoccupied electronic states with d and s symmetries. The $CeTa_3O_9$ spectrum shows a single strong 'white line' at the edge, typical of the Ce^{3+}-$4f^1$ state. In contrast, the CeO_2 spectrum shows two distinct peaks corresponding to the Ce^{4+}-$4f^0$ and Ce^{4+}-$4f^1\underline{L}$ configurations (where $\underline{L}$ denotes a ligand hole) (Soldatov *et al* 1994). As shown in figure 5, the Ce L_2-edge XANES spectra of both $(Sr_{0.8}Ce_{0.2})MnO_3$ and $(Sr_{0.8}Ce_{0.2})(Mn_{0.8}Co_{0.2})O_3$ show a bimodal feature and an edge shift towards higher energy from that of the Ce^{3+} standard, indicating that the Ce oxidation state in these two compounds is predominantly 4+. Our XANES results are similar to those reported for $(Ca_{0.8}Ce_{0.2})MnO_3$ (Zeng *et al* 2001).

Mn K-edge XANES spectra were also obtained from $(Sr_{0.8}Ce_{0.2})(Mn_{0.8}Co_{0.2})O_3$ and $(Sr_{0.8}Ce_{0.2})MnO_3$ (figure 6). Although the energy of the Ce L_1-edge (6549 eV) is very close to that of the Mn K-edge (6539 eV), the influence

of the Ce L_1-edge on the Mn K-edge spectra is negligible due to the significantly higher edge jump and fluorescence yield of the latter. The main feature at the Mn K-edge originates from dipole transitions of the Mn 1s core electrons into the unoccupied Mn 4p orbitals, and the energy of the absorption edge has been used to derive the Mn oxidation state in perovskite materials (Zeng *et al* 2001, Croft *et al* 1997). As shown in figure 6, Co-doping leads to a chemical shift of the Mn K-edge towards higher energy, indicating higher Mn valence in $(Sr_{0.8}Ce_{0.2})(Mn_{0.8}Co_{0.2})O_3$. This is consistent with the absence of JT-active Mn^{3+} ions in the Co-doped sample (see section 3.2, above).

3.4. Electrical conductivity

The total electrical conductivity was measured in air from 100 to 900 °C (figure 7), the values ranging from 150 to 300 and 25 to 100 S cm^{-1} for $(Sr_{0.8}Ce_{0.2})MnO_3$ and $(Sr_{0.8}Ce_{0.2})(Mn_{0.8}Co_{0.2})O_3$, respectively. The conductivity of $(Sr_{0.8}Ce_{0.2})MnO_3$ is in good agreement with previously reported values (Hashimoto and Iwahara 2000a). The temperature dependence of conductivity for these two samples can be described by the 'small polaron hopping' model with $\sigma \sim (1/T)\exp(-E_h/kT)$. The deduced activation energy for hopping (E_h) is 0.08 and 0.12 eV for $(Sr_{0.8}Ce_{0.2})MnO_3$ and $(Sr_{0.8}Ce_{0.2})(Mn_{0.8}Co_{0.2})O_3$, respectively. Our results are consistent with those reported by Lu *et al* (2005), who studied the resistivity of $(Sr_{0.8}Ce_{0.2})MnO_3$ at low temperatures (50–350 K). These authors fitted their resistivity data at $T < 250$ K with the 'variable range hopping (VRH)' model $\rho \sim \exp(T_0/T)^{1/4}$, and the same 'small polaron hopping' model at $T > 250$ K.

4. Conclusions

We have carried out a comparative study of $(Sr_{0.8}Ce_{0.2})MnO_3$ and $(Sr_{0.8}Ce_{0.2})(Mn_{0.8}Co_{0.2})O_3$ to investigate the effect of Co-doping using neutron diffraction, XANES and electrical conductivity measurements. Although the cooperative JT distortion was destroyed by Co-doping (which provides the necessary charge-compensation without reducing any Mn^{4+} to JT-active Mn^{3+} ions), the crystal structures and the phase transition behaviour remain essentially the same. At room temperature the structure for both compounds is tetragonal in space group $I4/mcm$ with a very similar octahedral tilt angle: 5.7° and 5.5° for $(Sr_{0.8}Ce_{0.2})MnO_3$ and $(Sr_{0.8}Ce_{0.2})(Mn_{0.8}Co_{0.2})O_3$, respectively. A continuous phase transition to cubic, due to the loss of octahedral tilting, was observed at 385 °C for $(Sr_{0.8}Ce_{0.2})MnO_3$ and 400 °C for $(Sr_{0.8}Ce_{0.2})(Mn_{0.8}Co_{0.2})O_3$. The temperature dependence of the tilt angle indicates that the transition is tricritical in nature for both samples. Furthermore, strain analysis suggests that the transition associated with the removal of JT distortion in $(Sr_{0.8}Ce_{0.2})MnO_3$ coincides with that from the loss of octahedral tilting. Although Ce-doping on the Sr-site is known to increase the conductivity of $SrMnO_3$ (Hashimoto and Iwahara 2000a), co-doping of Co on the Mn-site decreases the electrical conductivity. Therefore, $(Sr_{0.8}Ce_{0.2})MnO_3$ is a better candidate than $(Sr_{0.8}Ce_{0.2})(Mn_{0.8}Co_{0.2})O_3$ for potential cathode materials used in SOFC.

Acknowledgments

We acknowledge travel support to ISIS for ZZ, CJH and BJK from the Access to Major Research Facilities Programme (AMRFP), and to Taiwan for ZZ and BJK from the Australian Synchrotron Research Programme (ASRP). Both AMRFP and ASRP are funded by the Commonwealth of Australia. This work was partially supported by the Australian Research Council (ARC). The neutron facilities at ISIS are operated by the Science and Technology Facilities Council (STFC) with a contribution from the ARC. We are also grateful to Professor Michael Carpenter at the University of Cambridge for his advice on strain analysis, Dr Ronald Smith at Rutherford Appleton Laboratories for his assistance with the neutron diffraction experiments and Dr Ling-Yun Jang at NSRRC in Taiwan for his help with the XANES measurements.

References

Carpenter M A, Howard C J, Knight K S and Zhang Z 2006 Structural relationships and a phase diagram for (Ca, Sr)TiO_3 perovskites *J. Phys.: Condens. Matter* **18** 10725–49

Carpenter M A, Salje E K H and Graeme-Barber A 1998 Spontaneous strain as a determinant of thermodynamic properties for phase transitions in minerals *Eur. J. Mineral.* **10** 621–91

Chatterji T, Ouladdiaf B, Mandal P, Bandyopadhyay B and Ghosh B 2002 Jahn–Teller transition in $La_{1-x}Sr_xMnO_3$ in the low-doping region ($0 \leqslant x = 0.1$) *Phys. Rev.* B **66** 054403

Croft M, Sills D, Greenblatt M, Lee C, Cheong S W, Ramanujachary K V and Tran D 1997 Systematic Mn d-configuration change in the $La_{1-x}Ca_xMnO_3$ system: a Mn K-edge XAS study *Phys. Rev.* B **55** 8726

Dann T-E, Chung S-C, Huang L-J, Juang J-M, Chen C-I and Tsang K-L 1998 A high-performance double-crystal monochromator soft x-ray beamline *J. Synchrotron Radiat.* **5** 664–6

Glazer A M 1972 The classification of tilted octahedra in perovskites *Acta Crystallogr.* B **28** 3384–92

Hashimoto S and Iwahara H 2000a Structural, thermal and electrical properties of Ce-doped $SrMnO_3$ *J. Electroceram.* **4** 225–31

Hashimoto S and Iwahara H 2000b Study on the structural and electrical properties of $Sr_{1-x}Ce_xMnO_{3-\alpha}$ ($x = 0.1, 0.3$) perovskite oxide *Mater. Res. Bull.* **35** 2253–62

Howard C J, Zhang Z, Carpenter M A and Knight K S 2007 Suppression of strain coupling in perovskite $La_{0.6}Sr_{0.1}TiO_3$ by cation disorder *Phys. Rev.* B **76** 054108

Jin S, Tiefel T H, McCormack M, Fastnacht R A, Ramesh R and Chen L H 1994 Thousandfold change in resistivity in magnetoresistive La–Ca–Mn–O films *Science* **264** 413–5

Kennedy B J, Howard C J, Knight K S, Zhang Z M and Zhou Q D 2006 Structures and phase transitions in the ordered double perovskites $Ba_2Bi^{III}Bi^{V}O_6$ and $Ba_2Bi^{III}Sb^{V}O_6$ *Acta Crystallogr.* B **62** 537–46

Kennedy B J, Saines P J, Zhou Q, Zhang Z, Matsuda M and Miyake M 2008a Structural and electronic phase transitions in $Sr_{1-x}Ce_xMnO_3$ perovskites *J. Solid State Chem.* **181** 2639–45

Kennedy B J, Ting J, Zhou Q, Zhang Z, Matsuda M and Miyake M 2008b Structural characterisation of the perovskite series $Sr_{0.9-x}Ca_xCe_{0.1}MnO_3$: influence of the Jahn–Teller effect *J. Solid State Chem.* submitted

Kennedy B J and Zhou Q 2008 Sequential Jahn–Teller and tilting transitions in the mixed Ru Mn perovskite $SrRu_{0.5}Mn_{0.5}O_3$ *Solid State Commun.* **147** 208–11

Larson A C and von Dreele R B 1994 General structure analysis system (GSAS) *Los Alamos National Laboratory Report* LAUR 86-748

Lu W J, Zhao B C, Ang R, Song W H, Du J J and Sun Y P 2005 Internal friction evidence of uncorrelated magnetic clusters in electron-doped manganite $Sr_{0.8}Ce_{0.2}MnO_3$ *Phys. Lett.* A **346** 321–6

Maignan A, Martin C, Damay F and Raveau B 1998 Factors governing the magnetoresistance properties of the electron-doped manganites $Ca_{1-x}A_xMnO_3$ (A = Ln, Th) *Chem. Mater.* **10** 950–4

Mandal P, Hassen A and Loidl A 2004 Effect of Ce doping on structural, magnetic, and transport properties of $SrMnO_3$ perovskite *Phys. Rev.* B **69** 224418

Mathur N and Littlewood P 2003 Mesoscopic texture in manganites *Phys. Today* **56** 25–30

Negas T and Roth R S 1970 The system $SrMnO_{3-x}$ *J. Solid State Chem.* **1** 409–18

Rietveld H M 1969 A profile refinement method for nuclear and magnetic structures *J. Appl. Crystallogr.* **2** 65–71

Rodríguez-Carvajal J, Hennion M, Moussa F, Moudden A H, Pinsard L and Revcolevschi A 1998 Neutron-diffraction study of the Jahn–Teller transition in stoichiometric $LaMnO_3$ *Phys. Rev.* B **57** R3189

Salje E K H 1990 *Phase Transitions in Ferroelastic and Co-Elastic Crystals* (Cambridge: Cambridge University Press)

Skinner S J 2001 Recent advances in perovskite-type materials for solid oxide fuel cell cathodes *Int. J. Inorg. Mater.* **3** 113–21

Smith R I and Hull S 1997 User guide for the Polaris Powder Diffractometer at ISIS *Rutherford Appleton Laboratory Report* RAL-TR-97-038

Soldatov A V, Ivanchenko T S, Della Longa S, Kotani A, Iwamoto Y and Bianconi A 1994 Crystal-structure effects in the Ce L_3-edge x-ray-absorption spectrum of CeO_2: multiple-scattering resonances and many-body final states *Phys. Rev.* B **50** 5074

Sundaresan A, Tholence J L, Maignan A, Martin C, Hervieu M, Raveau B and Suard E 2000 Jahn–Teller distortion and magnetoresistance in electron doped $Sr_{1-x}Ce_xMnO_3$ ($x = 0.1$, 0.2, 0.3 and 0.4) *Eur. Phys. J.* B **14** 431–8

Toby B H 2001 EXPGUI, a graphical user interface for GSAS *J. Appl. Crystallogr.* **34** 210–3

Wu H Y, Ruan K Q, Huang S L, Lv Z M and Cao L Z 2007 Intrinsic inhomogeneity in the electron-doped manganite $Sr_{0.95}Ce_{0.05}MnO_3$ *Solid State Commun.* **141** 198–202

Zeng Z, Greenblatt M and Croft M 2001 Charge ordering and magnetoresistance of $Ca_{1-x}Ce_xMnO_3$ *Phys. Rev.* B **63** 224410

Zhang Z M, Howard C J, Kennedy B J, Knight K S and Zhou Q D 2007 Crystal structure of $Ln_{1/3}NbO_3$ (Ln = Nd, Pr) and phase transition in $Nd_{1/3}NbO_3$ *J. Solid State Chem.* **180** 1846–51